arXiv:2406.12912v1 [physics.ins-det] 13 Jun 2024

Prepared for submission to JINST

Burn-in Test and Thermal Performance Evaluation of Silicon Photomultipliers for the JUNO-TAO Experiment

---

X. Chen[a], G.F. Cao[b,c], M.H. Qu[d], H.W. Wang[b,*], N. Anfimov[e], A. Rybnikov[e], J.Y. Xu[b,c], A.Q. Su[d], Z.L. Chen[a], J. Cao[b], Y.C. Li[b], M. Qi[a]

[a]*Nanjing University,*
No.22 Hankou Road, Gulou District, Nanjing, Jiangsu 210093, China
[b]*Institute of High Energy Physics, Chinese Academy of Sciences,*
No.19B Yuquan Road, Shijingshan District, Beijing 100049, China
[c]*University of Chinese Academy of Sciences,*
No.1 Yanqihu East Rd, Huairou District, Beijing 101408, China
[d]*Zhengzhou University,*
No.100 Science Avenue, Zhengzhou, Henan 450001, China
[e]*Joint Institute for Nuclear Research,*
6 Joliot-curie str., Dubna, Moscow Region 141980, Russia

E-mail: wanghanwen@ihep.ac.cn

Abstract: This study evaluates more than 4,000 tiles made of Hamamatsu visual-sensitive silicon photomultipier (SiPM), each with dimensions of 5×5 cm^2, intended for the central detector of the Taishan Anti-neutrino Observatory (TAO), a satellite experiment of the Jiangmen Underground Neutrino Observatory (JUNO) aimed at measuring the reactor anti-neutrino energy spectrum with unprecedented energy resolution. All SiPM tiles underwent a room temperature burn-in test in the dark for two weeks, while cryogenic testing analyzed the thermal dependence of parameters for some sampled SiPMs. Results from these comprehensive tests provide crucial insights into the long-term performance and stability of the 10 square meters of SiPMs operating at -50°C to detect scintillation photons in the TAO detector. Despite some anomalies awaiting further inspection, all SiPMs successfully passed the burn-in test over two weeks at room temperature, which is equivalent to 6.7 years at -50°C. Results are also used to guide optimal SiPM selection, configuration, and operation, ensuring reliability and sustainability in reactor neutrino measurements. This work also provides insights for a rapid and robust quality assessment in future experiments that employ large-scale SiPMs as detection systems.

Keywords: Neutrino, Photon detectors, SiPM, Cryogenic detectors

ArXiv ePrint: 1234.56789

---

[*] Corresponding author.

Contents

1 Introduction 1

2 Experimental Setup 3
- 2.1 SiPMs for TAO 3
- 2.2 The Characterization Test in a Cryogenic Chamber 3
- 2.3 The Burn-in Test 4

3 Results and Discussions 5
- 3.1 Characterizations at Low Temperatures 5
- 3.2 Interpretation of the Burn-in Test Data 8

4 Summary 12

1 Introduction

The Taishan Antineutrino Observatory (TAO, also known as JUNO-TAO) is a satellite experiment of the Jiangmen Underground Neutrino Observatory (JUNO) [1]. It is a next-generation reactor neutrino experiment aimed at precise measurements of the neutrino energy spectrum and the exploration of potential new physics [2]. The TAO experiment is designed to position its detector, comprising 2.8 tons of Gadolinium-doped Liquid Scintillator (GdLS) and 4,024 Silicon Photomultiplier (SiPM) tiles covering a spherical area of nearly 10 m^2, in close proximity to one of the Taishan nuclear reactors. SiPMs are crucial components of the detector system, responsible for detecting faint scintillation light from neutrino interactions with a high photon detection efficiency of around 50%.

A number of dark matter and neutrino experiments, notably including DarkSide-20k and nEXO, utilize liquid-phase noble gases and employ large area of SiPMs serving as photo-detectors under cryogenic conditions. Significant progress has been achieved in detector development and SiPM testing, as documented in various studies [3–8]. To mitigate the dark noise in the SiPMs, the TAO detector is designed to operate at a temperature of -50°C (223K), adopting a new low-temperature liquid scintillator technology [9]. Given the critical importance of long-term sustainability, it is crucial to conduct studies on the thermal behavior of SiPMs, with a particular emphasis on burn-in tests. These tests are of great importance for detecting early failures and ensuring that the SiPMs' performance remains consistent over time, thus reinforcing the detector's reliability.

In our study, we subjected the SiPMs to a rigorous burn-in test at room temperature to comprehensively evaluate their stability and reliability. We recorded dark current and temperature over an extended period of approximately two weeks to identify potential failures and signs of degradation. Additionally, we systematically examined various SiPM parameters, such as breakdown voltage, dark count rate (DCR), and crosstalk, among others across different temperatures. These parameters were studied under cryogenic conditions within a specialized low-temperature chamber.

The dark current, denoted as I_{dark}, is a critical parameter in assessing the performance and reliability of SiPMs during the burn-in test. Our investigations have established that I_{dark} can be comprehensively represented as a function of temperature (T). This relationship stems from the fundamental insight that key factors influencing I_{dark}, such as the dark count rate (DCR), crosstalk (λ), and pixel gain (G_{pixel}), depend on temperature either directly or through their reliance on the temperature-sensitive breakdown voltage ($V_{\text{bd}}(T)$), or both. To accurately describe the dark current at room temperature, accounting for a small but non-negligible range of temperature variations, we use the following equation:

$$I_{\text{dark}} = G_{\text{pixel}} \cdot \frac{1}{1-\lambda} \cdot \text{DCR} \cdot e, \tag{1.1}$$

where G_{pixel} represents the gain of an individual SiPM pixel, λ denotes the crosstalk parameter, e is the elementary charge (1.602×10^{-19} C), DCR is the dark count rate, which can be further described by the temperature T and overvoltage V_{ov}:

$$\text{DCR} = \mathcal{S}(T) \cdot (V_{\text{ov}} - V_{\text{act.}}), \tag{1.2}$$

$$V_{\text{ov}} = V_{\text{bias}} - V_{\text{bd}}(T), \tag{1.3}$$

where $\mathcal{S}(T)$ is the slope of the DCR versus overvoltage and it only depends on the temperature T if we postulate a linear relationship between DCR and the overvoltage at a specified temperature, $V_{\text{act.}}$ represents the overvoltage threshold above which DCR begins to activate, V_{bias} is the bias voltage applied to the SiPM, and V_{bd} denotes the breakdown voltage. Furthermore, the breakdown voltage is subject to variations with temperature:

$$V_{\text{bd}}(T) = V_{\text{ref}} + (T - T_{\text{ref}}) \cdot \frac{dV_{\text{bd}}}{dT}, \tag{1.4}$$

in which V_{ref} and T_{ref} are reference values for the breakdown voltage and temperature, respectively. V_{ref} is determined with reference temperature $T_{\text{ref}} = 24°\text{C}$. We have also verified that there is a linear relation between V_{bd} and T (see Fig. 3 later on in the paper).

The pixel gain increases linearly with overvoltage as far as in the operating overvoltage range that we measured:

$$G_{\text{pixel}} = C_{\text{cell}} \cdot V_{\text{ov}} \tag{1.5}$$

where C_{cell} represents the capacitance of the SiPM cell. It is important to note that if G_{pixel} is expressed in number of electrons, then C_{cell} is considered in terms of capacitance; otherwise, it is a dimensionless coefficient.

The crosstalk parameter λ can be also approximated to have a linear relation towards overvoltage V_{ov}:

$$\lambda = \kappa \cdot (V_{\text{ov}} - \mathcal{V}_{\text{s}}) \tag{1.6}$$

In this equation, κ represents the slope, indicating the rate of change in λ with overvoltage, and $\mathcal{V}_{\text{s}}$ is the threshold overvoltage at which crosstalk begins to manifest.

It is important to note that the afterpulse effect is disregarded in Equation 1.1, as it only becomes significant at higher overvoltages (above 3.5 V) for the devices tested. The additional charge from afterpulsing is minimal; for instance, even at overvoltages of 6-7 V, it constitutes less than 2.5% of the charge of a single photon-electron for most of the tested devices. All of the conclusions above are based on testing results at -50°C. Our study shows that at higher temperatures, the afterpulse contribution decreases, making its impact even more negligible. Finally, the dark current model is formulated as:

$$I_{\mathrm{dark}}(T) = G_{\mathrm{pixel}}(V_{\mathrm{ov}}) \cdot \frac{1}{1-\lambda(V_{\mathrm{ov}})} \cdot \mathcal{S}(T) \cdot V_{\mathrm{ov}} \cdot e \tag{1.7}$$

2 Experimental Setup

To facilitate the mass testing of the SiPMs for TAO, we have developed and implemented a series of experimental setups. This article focuses on two key tests: the thermal dependence test, examining how SiPM performance varies with temperature, and the burn-in test, which evaluates SiPM performance at room temperature.

2.1 SiPMs for TAO

We employ the Hamamatsu MPPC S16088 with structure details discussed in Table 1 and the design shown in Figure 1, which integrates thirty-two 6 × 12 mm^2 chips into a single tile. Each pair of adjacent chips, together covering an area of 12 × 12 mm^2, constitutes a single channel. The design features a pixel pitch of 75 μm, with each chip hosting 12,782 pixels, achieving a photon-sensitive area coverage of 89.6%. Protecting the silicon sensor surface is a 0.65 ± 0.20 mm thick layer of epoxy resin with a refraction index of 1.54 for the blue light.

Table 1: **Structure details of the HPK S16088 SiPM.**

Parameters	Value	Unit
Number of channels	16 (4 × 4)	-
Effective photosensitive area	12 × 12	mm^2/ch.
Coverage of photosensitive area	89.6	%
Pixel pitch	75	μm
Number of pixels / channel	25,564	-
Window	Epoxy resin	-
Window refractive index	1.54	-

Given the compact design of the SiPM tile, each measuring 50.7 mm × 50.7 mm and comprising 16 channels for efficient arrangement, the central detector of the TAO project employs a total of 4024 such SiPM tiles.

2.2 The Characterization Test in a Cryogenic Chamber

Our experimental setup includes a customized stand for recording SiPM waveforms in dark, low-temperature conditions [10]. The testing platform resides within a cryogenic chamber, while the LED light source, power supply, and data acquisition (DAQ) system are located outside and

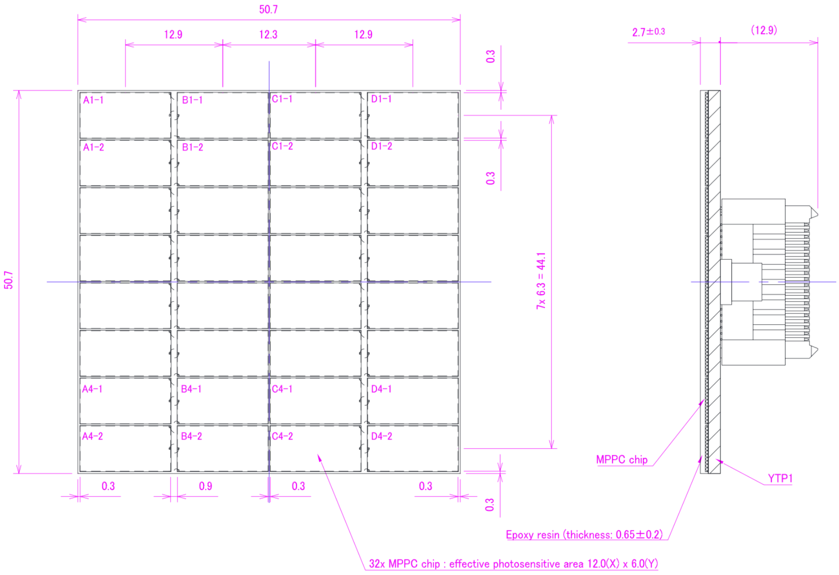
50.7
12.9
12.3
12.9
0.3
A1-1
B1-1
C1-1
D1-1
A1-2
B1-2
C1-2
D1-2
0.3
50.7
7x 6.3 = 44.1
A4-1
B4-1
C4-1
D4-1
A4-2
B4-2
C4-2
D4-2
0.3
0.9
0.3
0.3
0.3
2.7±0.3
(12.9)
MPPC chip
YTP1
Epoxy resin (thickness: 0.65±0.2)
32x MPPC chip : effective photosensitive area 12.0(X) x 6.0(Y)

Figure 1: Dimensional outline of the front and side view of the S16088 SiPM tile

connected via fibers and cables. The LED operates in pulse mode, generating weak illumination for the SiPMs. Additionally, we record waveforms under dark conditions to analyze the dark count rate of the SiPMs. This setup allows us to characterize the performance of SiPMs in a controlled, cryogenic environment, enabling precise measurements of their signal response and noise characteristics at low and varying temperatures. During each data acquisition session—referred to as a 'run'—sixteen SiPM tiles underwent simultaneous evaluation at a certain temperature, specifically after fully cooling down, ensuring that the system had reached thermal equilibrium.

2.3 The Burn-in Test

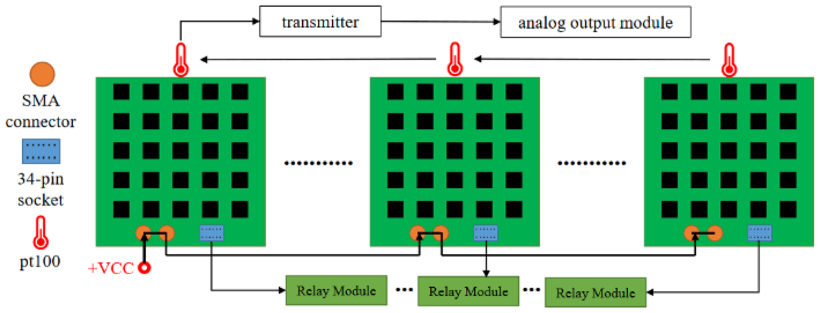
transmitter
analog output module
SMA connector
34-pin socket
pt100
+VCC
Relay Module
Relay Module
Relay Module

Figure 2: Experimental setup for the burn-in test featuring PCBs within a temperature-monitored dark chamber

The configuration of the burn-in test is depicted in Figure 2, showcasing 16 large printed circuit boards (PCBs) positioned inside a dark chamber that is regulated at room temperature.

This dedicated setup was designed and developed by another electronics team [11]. Each PCB is designed to accommodate 25 SiPM tiles, interconnected through Samtec connectors to facilitate easy and flexible replacement. The setup is equipped with PT100 sensors[12] for continuous ambient temperature monitoring. Each tile on these boards is subjected to around 54 V voltage for a duration of two weeks. We precisely measure the current of each tile using a Keithley 6487 picoammeter, coupled with relay modules for effective management of the testing channels.

3 Results and Discussions

3.1 Characterizations at Low Temperatures

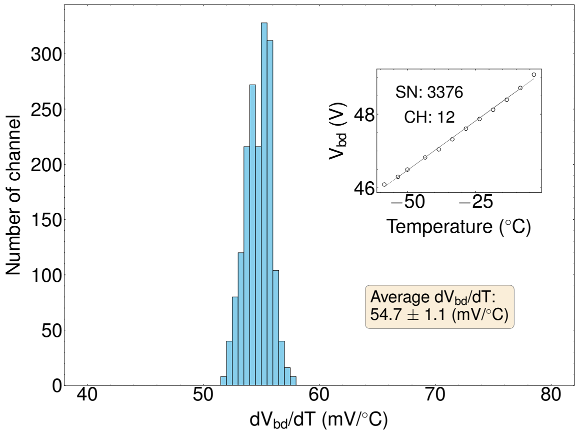

Figure 3: Breakdown voltage vs. temperature analysis for tested SiPMs: this figure illustrates the correlation between the breakdown voltage (V) and operating temperature (°C) across the SiPMs evaluated.

Breakdown Voltage As described in the methods section of the work [10], we collected waveforms for each SiPM at six preset over-voltages under LED illumination. To determine the single photo-electron (SPE) charge at a given over-voltage, we fitted the charge spectrum—derived from the waveforms within the LED illumination range—with Gaussian peaks. The difference between these peaks provided the SPE charge. Subsequently, the breakdown voltage for each SiPM was determined through a linear regression analysis of SPE charge as a function of the applied voltage. The breakdown voltage is indicated by the x-intercept, where the charge gain equals zero.

Figure 3 shows the correlation between the breakdown voltage and temperature for the tested SiPM channels, demonstrating that an increase in temperature corresponds to an elevation in breakdown voltage. The observed trend is quantitatively described by the slope of the linear regression, commonly referred to as the temperature coefficient of the breakdown voltage. For the selected SiPM channels in the test, this coefficient gives an average value of 54.7 ± 1.1 mV/°C with the consideration of non-uniformity. This result is fairly consistent with 54 mV/°C reported by Hamamatsu.

Dark Count Rate The DCR is determined through waveform analysis, wherein a specific threshold is applied to identify DCR pulses. The DCR for the Hamamatsu SiPM S16088 is initially computed for each channel, and then normalized by the channel's area (144 mm^2), resulting in a measurement expressed in Hz/mm^2. The analysis of the DCR as a function of temperature reveals critical insights into the behavior of our photodetector under varying thermal conditions.

In this study, we employ a model analogous to that presented by Collazuol et al. (2011) [13] and Aymeric et al. (2020) [14], the relationship between the DCR and temperature, incorporating the parameter of the energy gap E_g, which is formulated as

$$\mathrm{DCR}(T) = A_{\mathrm{amp}} \cdot T^{3/2} \cdot \exp(-E_g/kT) \tag{3.1}$$

In this equation, T represents the temperature in Kelvin, k is the Boltzmann constant, and E_g denotes the energy gap parameter, an intrinsic property that reflects the material's band structure. The coefficient A_{amp} is a device-specific parameter that scales the DCR amplitude.

Aligning with our linear approach to modeling DCR as a function of overvoltage, we prioritize presenting the slope $\mathcal{S}(T)$—defined as the rate of DCR alteration per volt derived from the linear fit—over direct DCR values. This strategy ensures consistency in our discussions and analysis. Figure 5a displays $\mathcal{S}(T)$ across a temperature scan ranging from -60°C to -20°C, well fit by the relation from Equation 3.1. This graph demonstrates how the DCR slope, derived from linearly fitting the DCR against overvoltage, varies with temperature for the selected SiPM. The analysis takes into account the non-zero activation voltage ($V_{\mathrm{act.}}$) at specific temperatures, adjusting the DCR-temperature relation by considering a 1 V overvoltage increment to account for temperature dependence of $V_{\mathrm{act.}}$, based on Equation 3.1. It is important to note that due to the pile-up effect observed when calculating DCR at higher temperatures (>-15°C) and higher overvoltages (>6V), the fit in the subsequent analysis does not include data affected by this effect. These data points are presented for illustrative purposes only.

It is important to note the potential temperature dependence of the energy gap, E_g. If E_g varies with temperature such that $E_g' = a + b \cdot T + c \cdot T^2$, this introduces a modification to the energy gap parameter. In this scenario, the temperature invariant term a, which is equal to E_g, represents the energy gap at a reference temperature. The term $b \cdot T$ merges into the amplitude parameter A_{amp} during the fitting process, while the term $c \cdot T^2$ is neglected due to the limitations in the precision of DCR measurement and the relatively negligible value of c. This approach accounts for the dynamic nature of the energy gap with varying temperatures.

The data plotted in Figure 5b originates from the linear fit analysis of DCR as a function of the overvoltage wherein the starting overvoltage $V_{\mathrm{act.}}$ is measured across difference temperatures for 256 SiPMs. We used box-and-whisker plots to illustrate non-uniformity, including contributions from potential uncertainties of DCR and the linear model, with extended error bars. The box represents values ranging from the 25th to the 75th percentile while the central black line indicates the median value. It's noted that precise determination of $V_{\mathrm{act.}}$ from room temperature burn-in data is challenging; hence, it's extrapolated over a range of temperatures from the cryogenic tests. There is a decreasing trend of $V_{\mathrm{act.}}$ with increasing temperature, although this trend is not clearly observable due to the large errors. Additionally, we assume that a negative overvoltage (biasing voltage below the breakdown voltage) should not yield a non-zero DCR. In the subsequent discussions involving room temperature results, we approximate the DCR as being proportional to the overvoltage without an intercept.

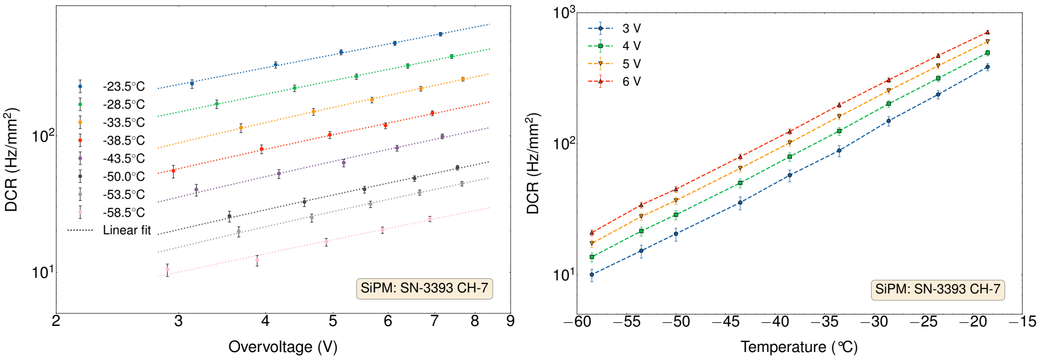

(a) (b)

Figure 4: (a) DCR versus overvoltage across various temperatures for a SiPM (b) Temperature dependence of DCR under varied overvoltages

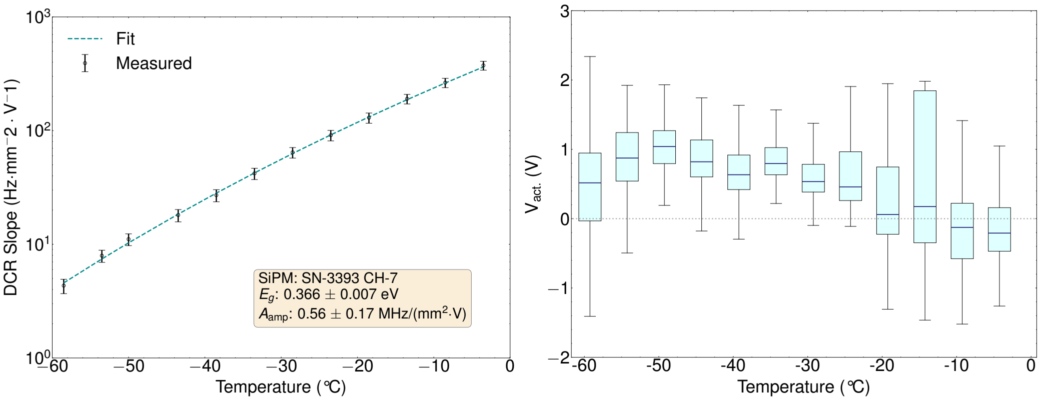

(a) (b)

Figure 5: (a) DCR v.s. overvoltage slope $\mathcal{S}(T)$ of the SiPM as a function of the temperature (left) (b) Baseline overvoltage $V_{\mathrm{act.}}$ for DCR activation of the tested SiPMs (right)

Through the analysis of 256 channels across 16 SiPM tiles, we fit the parameter E_g to our experimental data. The distribution of E_g, as depicted in Figure 6a, predominantly centralizes around 0.366 eV. This finding is consistent with the 0.36 eV reported in [13]. Figure 6b reveals the spread of amplitude A_{amp} values across various SiPMs. To ensure consistency and focus on the amplitude's variation, the energy gap (E_g) was fixed at 0.366 eV during the fit. It is important to recognize that the bandgap energy, E_g, may differ across devices due to variations in doping concentrations or the presence of defects. Determining E_g for each device, particularly under conditions of low temperatures, presents significant challenges. Therefore, we adopt a statistical approach to utilize E_g values for describing the dark current, I_{dark}, which will be elaborated upon subsequently.

Crosstalk Figure 7 shows how the crosstalk parameter, λ, varies with overvoltage for a SiPM at different temperatures for a specific SiPM. This parameter is derived by describing the number

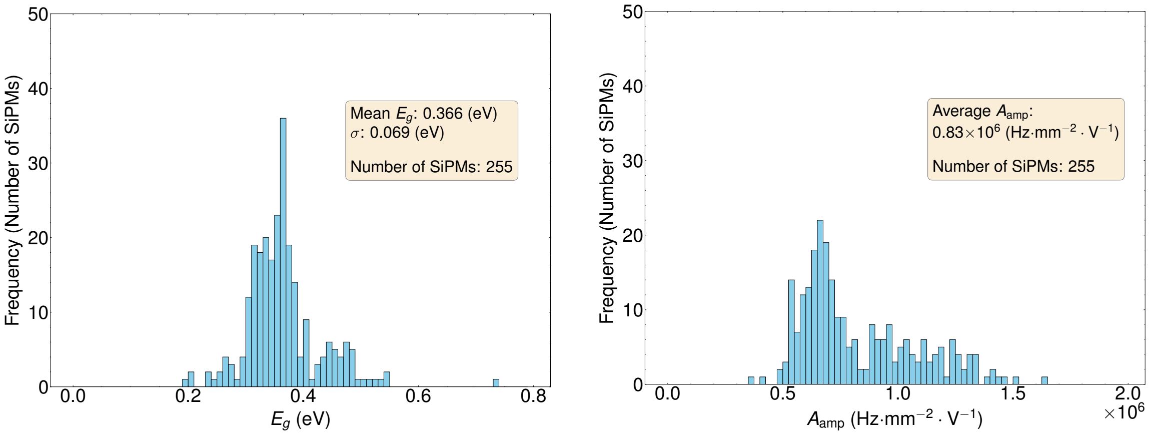

(a) Energy Gap (E_g) Distribution (b) Amplitude (A_{amp}) Distribution

Figure 6: (a) Energy gap (E_g) distribution from the fit (b) Amplitude (A_{amp}) distribution with fixed E_g

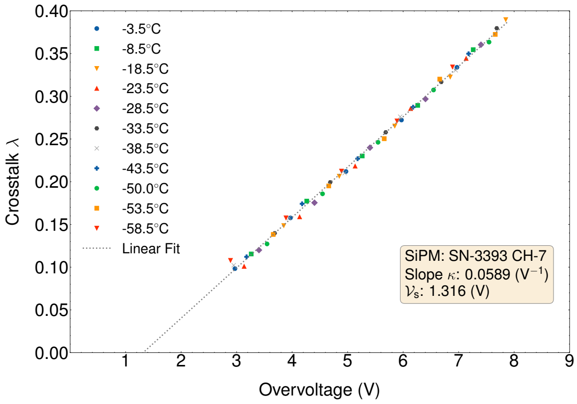

Figure 7: Variation of crosstalk parameter λ with overvoltage in a selected SiPM at different temperatures

of photon-electrons of pulses with a statistical model discussed in [15]. It is expected that λ demonstrates a linear correlation with overvoltage over a specific range and remains consistent across various temperatures. We conduct linear fits for all 256 SiPMs and obtain the average value of $\kappa = 0.0604$ V^{-1} and $\mathcal{V}_s = 1.264$ V, which are adopted to facilitate the description of the dark current in the following discussions. We made this approximation for two reasons: 1) the variations of κ and $\mathcal{V}_s$ mong different devices are small, and 2) it is not feasible to measure these values for all 64,000 SiPMs in over 4,000 SiPM tiles, given that we only obtained values for 256 SiPMs.

3.2 Interpretation of the Burn-in Test Data

We examined over 4,000 SiPM tiles in the burn-in test, periodically recording variations in current and temperature.

Dark Current Fit In our study, we describe the dark current by Equation 1.7 treating the breakdown voltage at the reference temperature (24°C) and the total current amplitude as two unconstrained parameters.

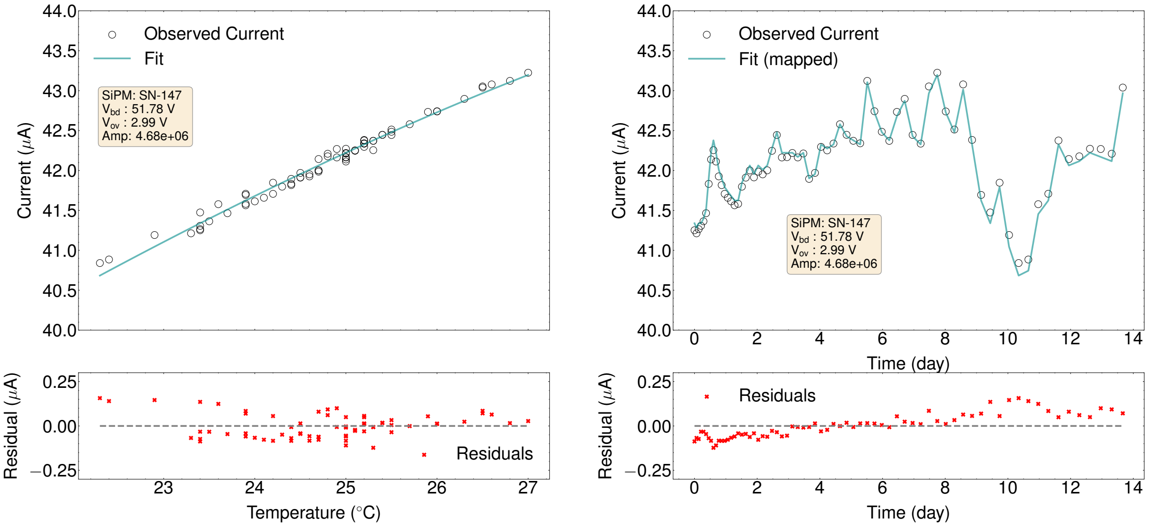

(a) (b)

Figure 8: Dark current model of temperature-only dependence: (a) Initial temperature fit showing how observed current values align with model predictions across different temperatures; (b) Corresponding translation of (a) where data and fit results are mapped to the recorded time.

Our model demonstrates a good fit to the burn-in data, accurately capturing the relationship between current and temperature, as illustrated in Figure 8a where the data points are well-aligned with temperature variations. Recognizing that temperature can fluctuate over time, we extended our analysis to examine the stability. This was achieved by mapping temperature $T(t)$ readings over time. Notably, we observed a slight increase in dark current as shown in the residuals of Figure 8b.

We consider that heat accumulation contributed to the increase in dark current over time, as the recorded temperature may not accurately reflect the actual temperature of the silicon sensors. Therefore, we introduce a time-dependent term to the dark current model as a temperature correction:

$$I_{\mathrm{t}}(t) = A_R \cdot \left(1 - \exp\left(-\frac{t}{\tau}\right)\right), \tag{3.2}$$

and subsequently, we modify the dark current model to include this term:

$$I'_{\mathrm{dark}}(T,t) = I_{\mathrm{dark}}(T) + I_{\mathrm{t}}(t), \tag{3.3}$$

where A_R represents the amplitude of this effect, and τ is the time constant associated with this process. Both A_R and τ serve as free parameters and are determined through a combined fit of the model to the data.

After incorporating the temperature correction over time, the fit describes the measured data more precisely, as illustrated in Figure 9a and 9b. The combined fit, incorporating both temperature and time variables, represents a two-dimensional analysis. Given the complexity of visualizing a

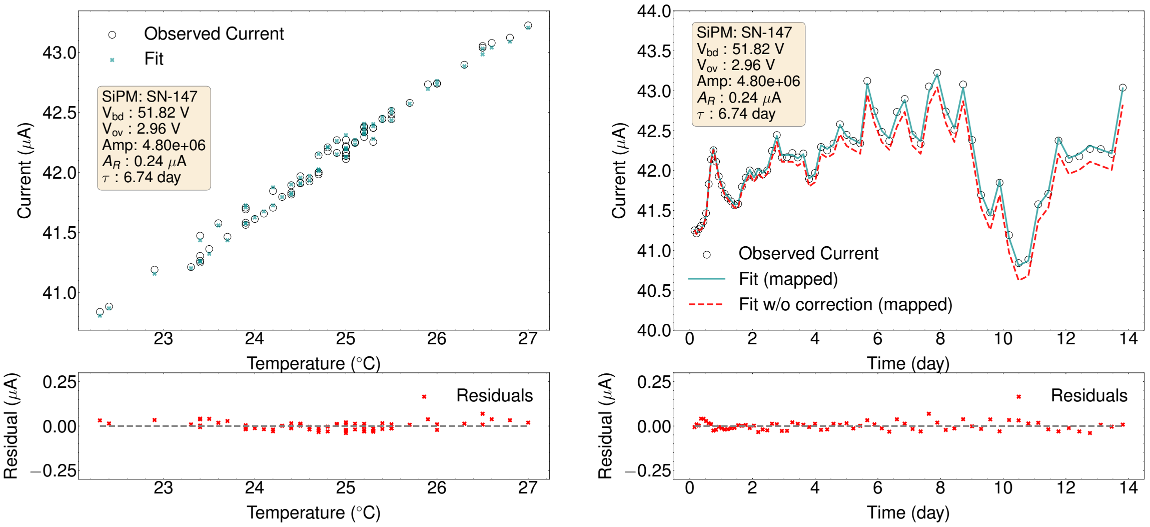

(a) (b)

Figure 9: Temperature-time-dependent model validation against burn-in data: (a) showcases the alignment between observed dark current values and those predicted by our temperature-time-dependent model across a range of temperatures, (b) depicts the dark current's time evolution, comparing measured values against those predicted by incorporating a time-dependent effect through $T(t)$.

2D fit in a single plot, we present the results separately: one plot for temperature and another for time, to enhance clarity. Additionally, a one-dimensional fit for temperature alone is included in Figure 9b, shown as a red dashed line, for comparison after being mapped to the recorded time. We also conducted a detailed examination on a subset of SiPMs that underwent the burn-in test on two separate occasions, as depicted in Figure 10. Each SiPM was initially subjected to the burn-in test, removed from the experimental setup, and subsequently reintroduced for a second test. The reiteration of the effect, with consistent levels of the parameters A_R and τ, suggests that what we observed is not attributable to permanent aging of the SiPM. Instead, it is more likely to reflect a transient, potential thermal inertia of the silicon sensors during the test.

We introduce a goodness-of-fit measure, $\chi^2 = \sum(\hat{I} - I)^2/(\sigma_x^2 + \sigma_y^2)$, to quantitatively assess the agreement between our model's predictions and the actual observed data. In this context, $\sigma_x = I_{\text{dark}}(T + T_{\text{unc.}}) - I_{\text{dark}}(T)$ accounts for the uncertainty in temperature measurements, where $T_{\text{unc.}} = 0.1$ °C reflects the precision of the temperature sensor and potential fluctuations. Meanwhile, σ_y represents the standard error associated with the measured currents. In this formulation, I denotes the observed dark currents, and $\hat{I}$ corresponds to the model's predictions. Figure 11 displays the χ^2 distribution across all SiPM tiles derived from the dark current modeling, alongside the Spearman rank correlation coefficients, which are calculated based solely on the temperature dependence of the dark current. We employ a χ^2 threshold of 6.5 and a correlation coefficient R_S of 0.8 as criteria to distinguish between normal and abnormal SiPM tiles, as well as to identify fit failures.

Following the application of these criteria, Figure 12 presents the distribution of dark currents for both normal and abnormal SiPM tiles. The dark current values are corrected to a reference

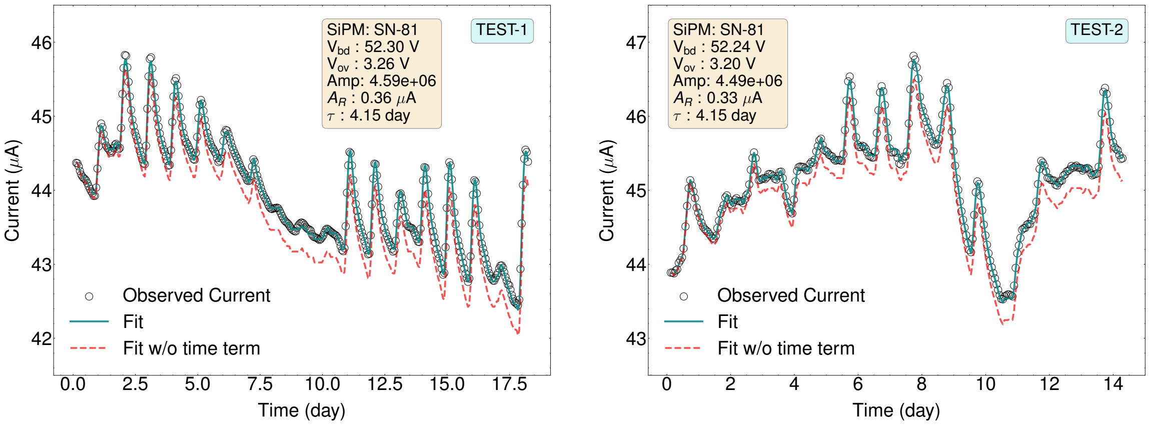

(a) First burn-in test

(b) Second burn-in test

Figure 10: Two distinct burn-in tests of the same SiPM

temperature of 24°C to facilitate direct comparison. Correction for normal SiPM tiles is applied using the fit model, whereas for the abnormal tiles, a linear temperature coefficient of current (dI/dT = 0.4752 μA/°C) derived from the normal tiles is used. This approach underscores the significant impact of thermal performance on dark current variability, with normal tiles displaying more consistent behavior than their abnormal counterparts. This analysis aids in identifying abnormal SiPM tiles that may require further examination.

Results of tested SiPM tiles are categorized by goodness-of-fit, correlation coefficient and dark current level in Table 2. In the examination of burn-in test data, approximately 350 SiPM tiles failed ($\chi^2 > 6.5$) to meet our goodness-of-fit criteria, though they demonstrated a dark current and temperature correlation ($R_S \geq 0.8$). Most of these tiles were associated with a particular testing session, during which there was an abrupt rise in environmental temperature, disrupting the subtle thermal equilibrium. Judging from the dark current level, approximately 11 SiPM tiles were also distinguished as anomalies due to their high dark current ($\geq$ 100 μA) behaviour, yet they still exhibited a consistent current-temperature correlation. These tiles have been marked for further investigation.

The current and temperature data along the timeline for two distinct SiPMs: one exhibiting normal behavior (good current and temperature correlation) and one exhibiting abnormal behavior (poor current and temperature correlation), are shown in Figure 13a and 13b.

We also conducted a linear comparison between the breakdown voltage, $\mathrm{V}_{\mathrm{bd}}^{\mathrm{burnin}}$, derived from burn-in data fitting, and the estimated breakdown voltage, $\mathrm{V}_{\mathrm{bd}}^{\mathrm{est.}}$, extrapolated from cryogenic test results. This analysis includes 16 SiPM tiles, excluding one due to abnormal behavior. As shown in Figure 14, linear fitting reveals a strong correlation between $\mathrm{V}_{\mathrm{bd}}^{\mathrm{burnin}}$ and $\mathrm{V}_{\mathrm{bd}}^{\mathrm{est.}}$, evidenced by a Pearson correlation coefficient of 0.889. The difference in breakdown voltage is 0.203 ± 0.073 V at a baseline $\mathrm{V}_{\mathrm{bd}}^{\mathrm{burnin}}$ of 51.5 V.

Finally, assuming constant charge endurance and negligible pixel gain variation with temperature, we calculate the equivalent operating time using Equation 3.1 with E_g = 0.366 eV, as shown in Figure 15. The equivalent operating time at -50°C for a two-week burn-in test at 24°C is 2461.5 days (6.7 years).

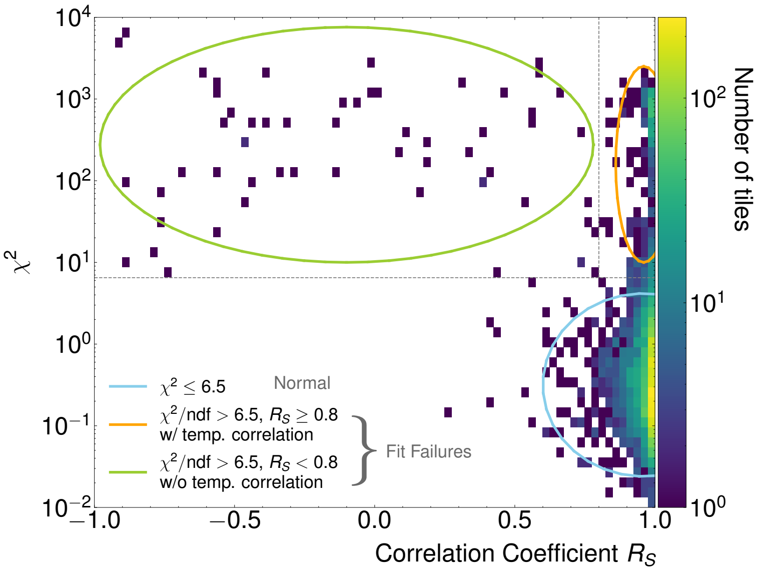

Figure 11: Distribution of χ^2 Values and Spearman's Rank Correlation Coefficients for SiPM Tiles Based on Dark Current Modeling. This figure categorizes SiPM tiles into three distinct clusters based on their thermal performance: normal, abnormal, and fit failures.

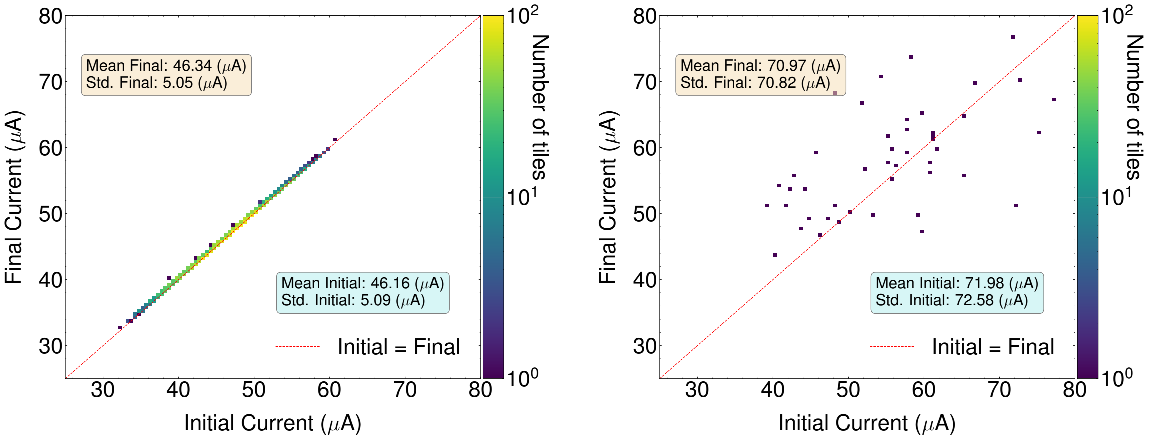

(a) Normal SiPM tiles showing a tight distribution of dark currents ($\chi^2 \leq 6.5$)

(b) Abnormal SiPM tiles with a wide distribution of dark currents ($\chi^2 > 6.5 \cap R_S < 0.8$)

Figure 12: Comparison of dark current distributions for normal and abnormal SiPM tiles at a normalized average temperature.

4 Summary

This study presents the findings from both the SiPM burn-in test and characterizations within a cryogenic environment. Although the burn-in data (current, temperature, time) are limited in scope, we successfully derived meaningful insights using a specialized dark current model, incorporating

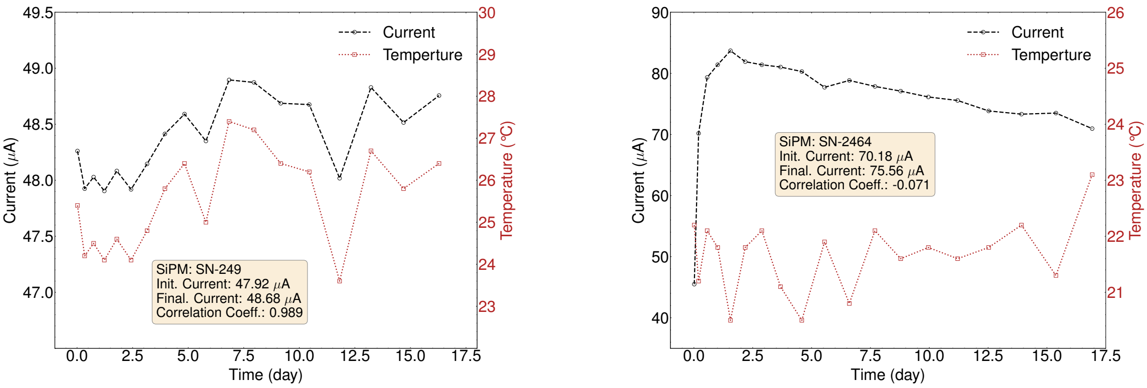

(a) Normal (b) Abnormal

Figure 13: Comparative illustration of temperature and dark current variations over time for normal and abnormal SiPM tiles.

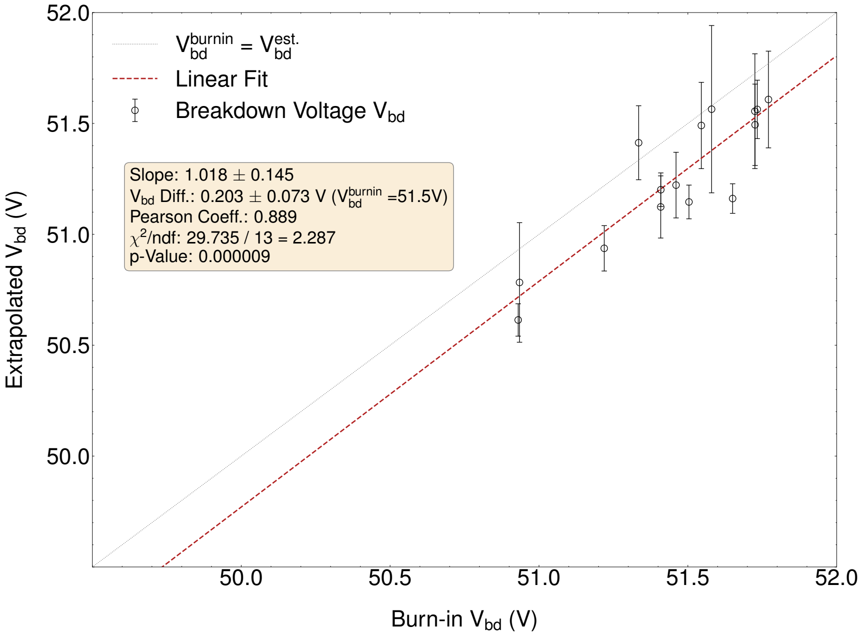

Figure 14: Linear Comparison of Breakdown Voltage (V_{bd}) from Burn-in Data and Cryogenic Test Extrapolation

several critical parameters. The dark current model effectively fits the burn-in data and yields acceptable chi-square (χ^2) values for most tiles. We also employed a robust approach to examine the current-temperature correlation with Spearman coefficients to account for the fit failures. A temperature correction is also developed to account for potential thermal inertia. Additionally, we discovered that the breakdown voltage—determined through the burn-in dark current model—aligns closely with traditional methods that extrapolate based on temperature.

Furthermore, we assess the dark current at room temperature of more than 4,000 SiPM tiles,

Table 2: Overview of dark current levels and classification of SiPM tiles based on goodness-of-fit and temperature correlation

Category \ Dark Current (μA)	[0, 30)	[30, 60)	[60, 100)	≥100	Total
Fit Success ($\chi^2 \leq 6.5$)					
Normal	0	3597	1	0	3598
Fit Failure ($\chi^2 > 6.5$)					
w/ Temperature Correlation ($R_S \geq 0.8$)	1	347	1	11	360
w/o Temperature Correlation ($R_S < 0.8$)	0	30	27	2	59
Total	1	3974	29	13	4017

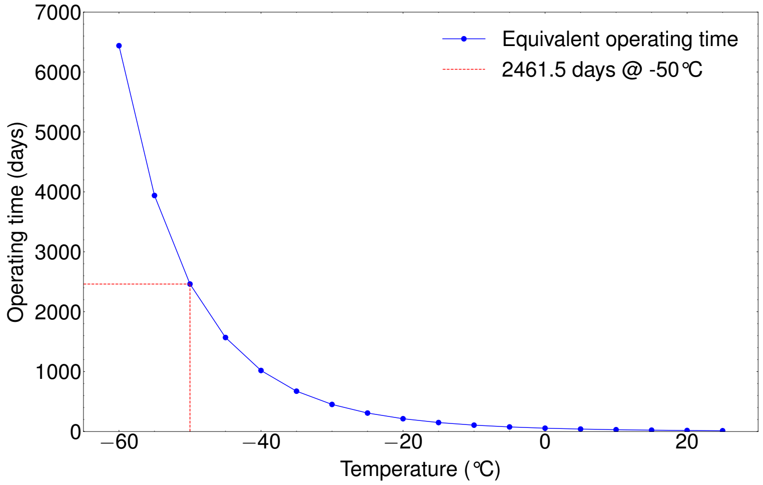

Figure 15: Equivalent operating time at various temperatures for a two-week burn-in test at room temperature (24°C).

which together provide a photon-sensitive surface area of nearly 10 m^2. Our analysis finds that the majority of the SiPM tiles exhibit dark current levels (I_{dark}) ranging between 30 to 60 μA. Nonetheless, we identify anomalies among the 4,000 SiPM tiles. We find 13 tiles with dark current values exceeding 100 μA, higher than the norm, whereas 59 tiles demonstrated poor correlation between dark current and temperature. These anomalous SiPM tiles are slated for further inspection at the cryogenic testing facility to understand how their peculiar behavior during the burn-in test affects key performance parameters. Despite the presence of anomalies, all SiPMs successfully passed the two-week burn-in test at room temperature, which is equivalent to an operation time of 6.7 years at -50°C.

Acknowledgments

We gratefully acknowledge support from the RSF-NSFC Cooperation Funding under Grant No. 12061131008.

References

[1] F.A. et al, *Neutrino physics with juno*, *J. Phys. G: Nucl. Part. Phys.* **43** (2016) 030401.

[2] JUNO Collaboration, A. Abusleme, T. Adam, S. Ahmad, S. Aiello, M. Akram et al., *Tao conceptual design report: A precision measurement of the reactor antineutrino spectrum with sub-percent energy resolution*, 2020.

[3] C. Guo, M. Guan, X. Sun, W. Xiong, P. Zhang, C. Yang et al., *The liquid argon detector and measurement of sipm array at liquid argon temperature*, *Nuclear Instruments and Methods in Physics Research Section A: Accelerators, Spectrometers, Detectors and Associated Equipment* **980** (2020) 164488.

[4] L. Wang, M. Guan, H. Qin, C. Guo, X. Sun, C. Yang et al., *Characterization of vuv4 sipm for liquid argon detector*, *Journal of Instrumentation* **16** (2021) P07021.

[5] L. Baudis, M. Galloway, A. Kish, C. Marentini and J. Wulf, *Characterisation of silicon photomultipliers for liquid xenon detectors*, *Journal of Instrumentation* **13** (2018) P10022.

[6] G. Gallina, P. Giampa, F. Retière, J. Kroeger, G. Zhang, M. Ward et al., *Characterization of the hamamatsu vuv4 mppcs for nexo*, *Nuclear Instruments and Methods in Physics Research Section A: Accelerators, Spectrometers, Detectors and Associated Equipment* **940** (2019) 371.

[7] G. Gallina, Y. Guan, F. Retiere, G. Cao, A. Bolotnikov, I. Kotov et al., *Performance of novel vuv-sensitive silicon photo-multipliers for nexo*, *The European Physical Journal C* **82** (2022) 1125.

[8] Z. Balmforth, A. Basco, A. Boiano, N. Canci, R. de Asmundis, F.D. Capua et al., *A large facility for photosensors test at cryogenic temperature*, *Journal of Instrumentation* **18** (2023) C03024.

[9] Z. Xie, J. Cao, Y. Ding, M. Liu, X. Sun, W. Wang et al., *A liquid scintillator for a neutrino detector working at* -50 *degree*, *Nuclear Instruments and Methods in Physics Research Section A: Accelerators, Spectrometers, Detectors and Associated Equipment* **1009** (2021) 165459.

[10] A. Rybnikov, N. Anfimov, M. Qu, A. Chetverikov, G. Cao, D. Fedoseev et al., *Performance of the mass testing setup for arrays of silicon photomultipliers in the tao experiment*, 2024.

[11] S. Xia, P. Hu, Y. Zhang, S. Qian, G. Cao and J. Yang, *Design and implementation of sipm burn-in test experimental system for tao detector*, *Radiation Detection Technology and Methods* (2023) .

[12] VWR International, LLC., "Precision PT100 reference sensors." `https://sg.vwr.com/store/product/804738/precision-pt100-reference-sensors`, 2024.

[13] G. Collazuol, M. Bisogni, S. Marcatili, C. Piemonte and A. Del Guerra, *Studies of silicon photomultipliers at cryogenic temperatures*, *Nuclear Instruments and Methods in Physics Research Section A: Accelerators, Spectrometers, Detectors and Associated Equipment* **628** (2011) 389.

[14] A. Panglosse, P. Martin-Gonthier, O. Marcelot, C. Virmontois, O. SaintPé et al., *Dark count rate modeling in single-photon avalanche diodes*, *IEEE Transactions on Circuits and Systems I: Regular Papers* **67** (2020) 1507.

[15] S. Vinogradov, *Analytical models of probability distribution and excess noise factor of solid state photomultiplier signals with crosstalk*, *Nuclear Instruments and Methods in Physics Research Section A: Accelerators, Spectrometers, Detectors and Associated Equipment* **695** (2012) 247.